PIER C

(Received 25 January 2026, Accepted 19 February 2026, Scheduled 2 April 2026)

Suppressing Torque Ripple of PMa-SRM Based on Variable Hysteresis Threshold in Sub-Divided Region

Junwu Zhu, Junxin Xu*, and Yan Chen

School of Electrical Engineering and Automation, Jiangxi University of Science and Technology, Ganzhou 341000, Jiangxi, China

ABSTRACT: To address the issue of significant torque ripple in traditional direct instantaneous torque control strategies for permanent magnet assisted switched reluctance motors, which stems from the use of fixed hysteresis thresholds, this paper proposes a variable hysteresis threshold pulse width modulation (PWM) method based on subdivided regions. First, based on the torque-current ratio curve features, the two-phase exchange (TpE) region is subdivided into two-phase exchange I (TpE I) and two-phase exchange II (TpE II), using the angle of equal torque-current ratio as the dividing point. PWM control was applied within these two intervals to ensure a smoother transition of the total torque during commutation. Second, the hysteresis threshold is optimized by a BP neural network tuned via the dung beetle optimizer (DBO) algorithm under different speeds and loads, thereby enhancing the system's flexibility. Finally, simulations and experiments were performed using a 6/20 three-phase permanent magnet-assisted switched reluctance motor. Experimental results show that the torque ripple is reduced from 30.4% to 11% under 500 r/min and 5 N · m, and PWM with a variable hysteresis threshold can effectively suppress torque ripple.

1. INTRODUCTION

Permanent magnet-assisted switched reluctance motor (PMa-SRM) integrates the advantages of both a permanent magnet synchronous motor, owing to its high power density, and a switched reluctance motor, with its simple structure and wide speed range. It makes them particularly suitable for applications in electric vehicles, high-end home appliances, and precision servo systems [1–3]. However, owing to its double-salient-pole structure, nonlinear magnetic circuit, and the phase-split excitation characteristics, the motor still exhibits significant torque ripple and acoustic noise during operation, hindering its broader application [4].

Numerous control strategies have been developed to suppress torque ripple. Current control methods include Current Chopper Control (CCC) and Model Predictive Control (MPC) [5–8]; torque control techniques include Direct Instantaneous Torque Control (DITC), Direct Torque Control (DTC), and Torque Sharing Function (TSF) [9–12].

Hysteresis control and interval division techniques are extensively employed in current and torque control systems. In DITC, the switching of the motor windings is governed directly by the fixed hysteresis controller, which processes the instantaneous torque error and rotor position. This approach reduces the complexity of the control method [13–15]. However, it is incapable of significantly mitigating torque ripple during commutation transitions. To reduce torque ripple, [16] proposes an adaptive hysteresis threshold strategy that automatically adjusts the threshold based on motor speed and back-EMF (electromagnetic field). However, the measurement of back-EMF in the PMa-SRM presents difficulties. In [17], the author proposes an optimized strategy based on a fixed hysteresis current controller, aiming to resolve the trade-off between torque ripple and switching losses in traditional brushless direct current (BLDC) motor control, achieving simultaneous minimization of both. In [18, 19], the authors employ the Dung Beetle Optimizer (DBO) algorithm to enhance traditional approaches. This facilitates precise motor loss estimation and adaptive tuning of control parameters, which collectively confirm the algorithm's efficacy. The method in [20] divides the commutation phase into two regions according to the inductance profile and employs a distinct hysteresis control strategy in each. In [21], an optimization algorithm is used to adjust the turn-on and turn-off angles, thereby rapidly increasing the incoming phase current and decreasing the outgoing phase current. The PWM technique with DITC proposed in [22, 23] reduces torque ripple and current peak by implementing distinct control strategies in each operational interval. An analytical segmented PWM duty cycle method for switched reluctance motors is presented in [24]. By calculating the duty cycle independently for each inductance zone, the method regulates the phase voltage to effectively suppress current peaks and torque ripple. In [25], a DITC approach integrating hysteresis threshold control with PWM was introduced. The aforementioned references adopt fixed hysteresis or single-hysteresis control methods, in which the hysteresis threshold and region division fail to achieve coordinated control and optimization. The control method proposed in this paper combines the subdivision of operating regions with adaptive adjustment of the hysteresis threshold simultaneously, thereby achieving superior comprehensive performance.

In response to the significant torque ripple issue in the traditional DITC with fixed hysteresis threshold strategy, this study

* Corresponding author: Junxin Xu (xujx9997@163.com).

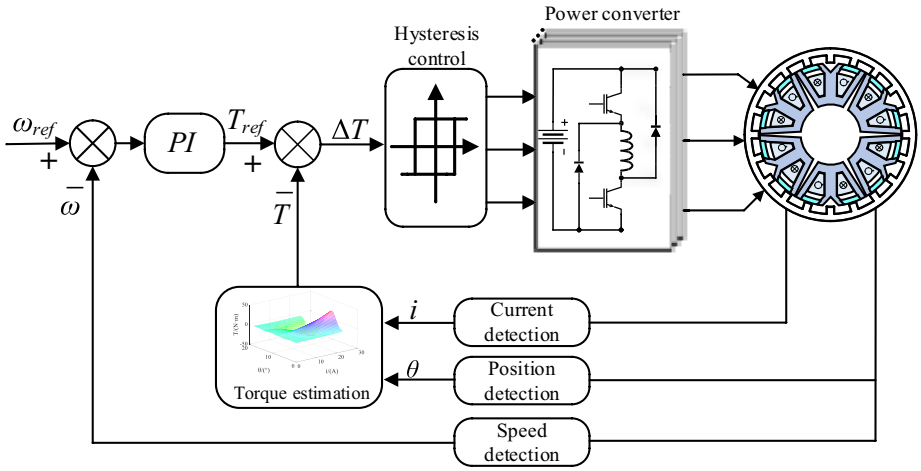

FIGURE 1. Traditional control diagram of DITC.

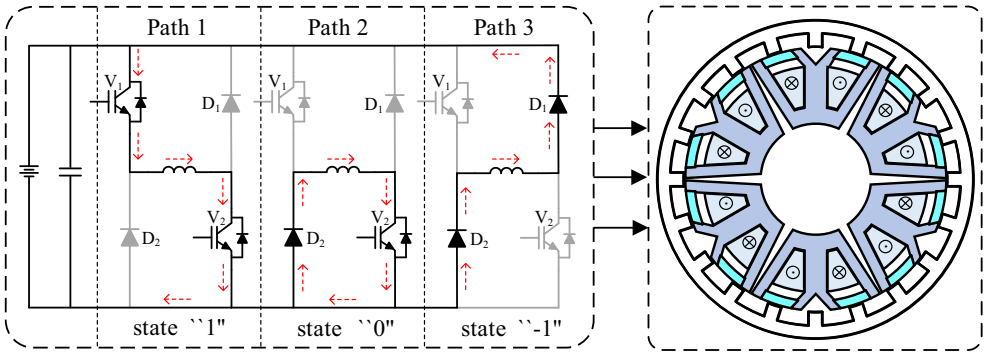

FIGURE 2. Asymmetric half-bridge and switching state.

proposes a variable hysteresis threshold torque ripple suppression strategy based on the subdivided region of the torque-to-current ratio. In addition, the DBO algorithm is integrated to optimize the back propagation (BP) neural network (DBO-BP) for predicting the hysteresis threshold. A motor model was built and simulated, and prototype experiments were performed using a three-phase 6/20 PMa-SRM to validate the proposed method.

2. TRADITIOANAL DITC STRATEGY

As shown in Figure 1, the torque error was calculated by comparing the actual output torque with the reference torque generated by the power integral (PI) speed controller in the traditional DITC strategy. Subsequently, the state of the power switch is determined based on the magnitude of the torque error and the threshold value of the hysteresis controller, which controls the switching of each phase winding.

The reluctance torque expression for the permanent magnet-assisted synchronous reluctance motor can be formulated in (1).

$$T_e = \frac{1}{2} i_k^2 \frac{\partial L_k}{\partial \theta} \tag{1}$$

where T_e, i, L, and θ represent torque, current, inductance, and position angle, respectively.

The permanent magnet torque is defined by the following Equation (2).

$$T_p = i_k \frac{d\psi_k}{d\theta} \tag{2}$$

The total torque of the PMa-SRM can be derived from Equations (1) and (2) as:

$$T_{total} = \frac{1}{2} i_k^2 \frac{\partial L_k}{\partial \theta} + i_k \frac{d\psi_k}{d\theta} \tag{3}$$

where L is the inductance, and ψ denotes the flux linkage.

As shown in Equation (3), the PMa-SRM incorporates permanent magnet torque into the traditional reluctance torque, thereby reducing the magnetic reluctance torque component that is proportional to the square of the current. By modulating the current amplitude, the distribution between reluctance torque and permanent magnet torque can be flexibly controlled across various operating speeds and loads.

The three-phase power converter is built using an asymmetric half-bridge structure, as shown in Figure 2. Each bridge arm works independently and consists of two insulated-gate bipolar transistors (IGBTs) and two freewheeling diodes for current commutation. The excitation and de-excitation of each phase winding are controlled by modulating the state of the IGBTs.

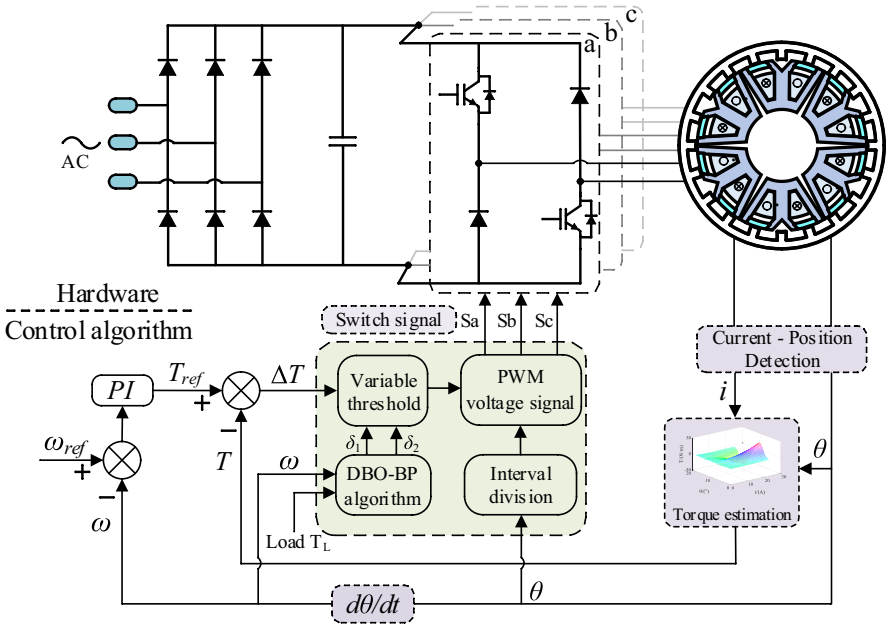

FIGURE 3. Control diagram of the proposed.

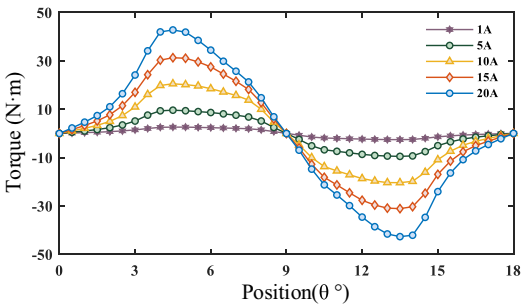

FIGURE 4. Torque distribution in one rotor electrical period.

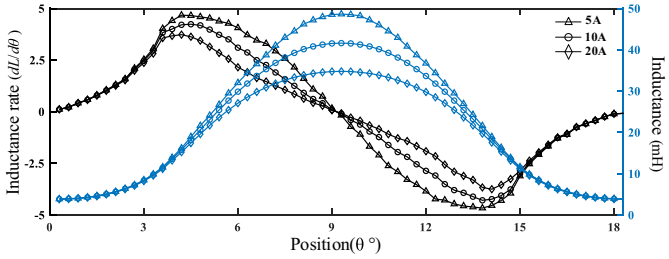

FIGURE 5. Distribution diagram of inductance and inductance rate.

The switching operation of each pair of IGBTs on the bridge arm generates three distinct switching states. Taking the A phase winding as an example, for path 1: both the upper tube V_1 and lower tube V_2 are excited, and the positive voltage is applied across the winding terminals; the state is "1", and the current increases rapidly. For path 2: the V_1 is turned off and V_2 turned on, and the winding begins with the initial current at the instant of turn-off and circulates through the V_2-D_2 loop; the state is "0", and the current decreases slowly. For path 3: Both V_1 and V_2 are turned off, causing the current to decrease fast through the motor winding, D_1, D_2, and the power supply, forming a closed loop. The negative voltage is applied across the terminals of the motor windings, resulting in reverse demagnetization and a rapid decrease of the current that is state "-1".

The value of the hysteresis threshold keeps constant in the traditional DITC control strategy. The torque error is compared with the upper and lower limits of the hysteresis threshold at some special rotor position angle to control IGBTs, thereby regulating the energization of each phase winding. However, this strategy lacks a mechanism for dynamically adjusting the hysteresis threshold and fails to account for the influence of the motor's torque-angle characteristics on the hysteresis threshold. Consequently, a lag occurs during commutation, resulting in significant torque ripple in the motor.

3. INTERVAL CONTROL METHOD WITH VARIABLE HYSTERESIS THRESHOLD

An appropriate selection of the hysteresis threshold is essential for ensuring the stability of the control system. In this study, the DBO algorithm was employed to optimize the BP neural network, refining the hysteresis threshold. In addition, PWM was integrated with the DITC to enhance the flexibility of the control system. The block diagram illustrating the control principle is shown in Figure 3.

3.1. Interval Division Based on Torque-Current Ratio

The torque output capability of each phase is influenced by the rotor position, as shown in Figures 4 and 5. This paper presents a torque ripple mitigation method for the PMa-SRM that utilizes its nonlinear inductance characteristics to improve operational efficiency across a wide range of operating conditions. Specifically, the torque-current ratio approach is employed to

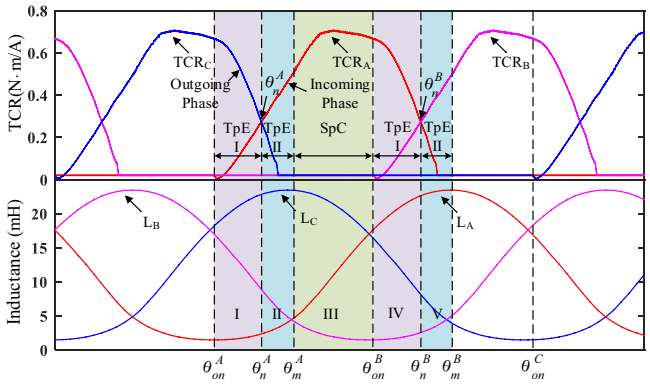

FIGURE 6. Region division based on torque-current ratio.

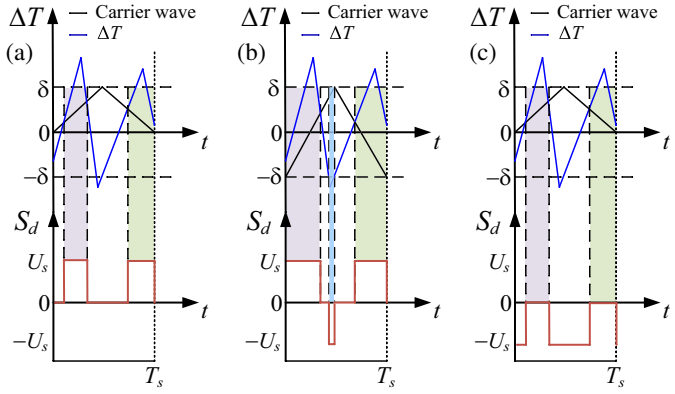

FIGURE 7. PWM control. (a) I region; (b) II, III, IV regions; (c) V region.

partition the rotor position into distinct regions within one cycle.

According to the torque formula (1), the torque-current ratio (TCR) equation can be formulated.

$$TCR = \frac{T_k}{i_k} = \frac{1}{2} i_k \frac{dL_k}{d\theta} \tag{4}$$

It shows that the torque-current ratio is proportional to the rate of inductance change, which reflects the torque output capability of each phase winding.

In Figure 6, during the first half of the commutation process, the outgoing phase exhibits a higher torque-current ratio, resulting in a greater electromagnetic torque output than the incoming phase. In the latter half of the commutation process, the torque-current ratio of the incoming phase surpasses that of the outgoing phase, thereby contributing primarily to the torque output. Consequently, the position angle θ_n, at which the torque-current ratios of the incoming and outgoing phases are equal, is selected as the boundary point, and the torque output characteristics of both the incoming and outgoing phases can be clearly delineated. Based on this, the two-phase exchange region of the motor is divided into Two-Phase Exchange I (TpE I) and Two-Phase Exchange II (TpE II).

Taking A phase as an example. The turn-on angle θ^A_{on} that is 0 degrees in this work of PMa-SRM is defined as the starting point of TpE I. The angular position θ^A_n, where the torque-current ratios of the two phases are equal, serves as both the endpoint of TpE I and the starting point of TpE II. Angle θ^A_m as the endpoint of TpE II corresponds to the starting point of the single-phase conducting (SpC), which is the fixed angular position, where the rotor leading edge coincides with the stator leading edge. As shown in Figure 6, when the A phase is used as the incoming phase, its TpE I, II, and SpC regions are denoted as I, II, and III, respectively. When it is used as the outgoing phase, its TpE I and II regions are denoted as IV and V, respectively.

3.2. PWM Control of Sub-Divided Region

To address the issue wherein the hysteresis controller retains its state from the previous hysteresis interval within the hysteresis range but continuously modifies its output state outside this range in response to the torque error, the traditional fixed hysteresis is replaced with the variable hysteresis and integrated with the PWM algorithm. Additionally, distinct torque-error hysteresis thresholds were established for varying torque-current ratio intervals. The corresponding PWM duty cycle is determined based on the instantaneous torque error, and appropriate switching signals for each phase winding are generated. The instantaneous torque error ΔT is defined in (5).

$$\Delta T = T_{ref} - T \tag{5}$$

where T_{ref} and T represent the reference torque and actual torque, respectively.

As shown in Figure 6, region I is a small inductance zone that requires rapid energization, whereas region V is the position where the stator and rotor are about to align and require rapid demagnetization to prevent negative torque generation. A unipolar triangular carrier is compared with the torque error ΔT in regions I and V as shown in Figures 7(a) and (c), respectively, which show that the torque error curve is relatively slow. This can increase the duration of energization and demagnetization. The rate of change of inductance gradually increases and stabilizes in regions II, III, and IV, and the change in current affects the torque output from Equation (1). The bipolar triangular carrier was compared with the torque error ΔT in regions II, III, and IV as shown in Figure 7(b), which is capable of switching between the positive and negative axes and provides a faster response to the torque error curve. It enables the precise adjustment of the duty cycles for the "1, 0, -1" voltage levels to regulate current, thereby steadily maintaining the torque output.

The PWM control method for region I is shown in Figure 7(a). The motor requires rapid energization in region I, and the switching states are limited to "1" and "0", so when $\Delta T > \delta$, the actual torque is small; then, the switching state is "1". When $\Delta T < \delta$, the switching state is "1" if ΔT is greater than the triangular carrier wave, and the switching state is "0" if ΔT is less than the triangular carrier.

The PWM control methods for regions II, III, and IV are shown in Figure 7(b). In these three regions, the rate of inductance change began to increase and gradually stabilized, undertaking the main torque output of the motor. To maintain a stable torque output, the switching states alternate among "1,

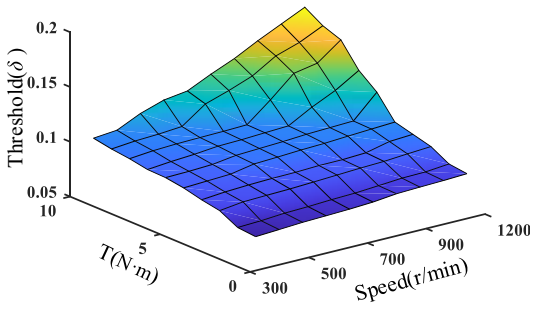

FIGURE 8. The variation of the threshold with speed and load.

0, −1". When $\Delta T > \delta$, the actual torque is not sufficient, and the switching state is "1" to increase torque output. When $-\delta \leq \Delta T \leq \delta$, the actual torque is close to the reference torque, and the switching state is "1" if ΔT is greater than the triangular carrier wave; the switching state is "0" if ΔT is less than the triangular carrier wave. When $\Delta T < -\delta$, the actual torque output is high, and the switching state is "−1" to reduce torque output.

The PWM control method for region V is shown in Figure 7(c). The motor operates in the V region, which rapidly demagnetizes to reduce the current to zero, and the switching states are limited to "0" and "−1". When $\Delta T > \delta$, the actual torque is small, but motor operates in the demagnetization phase, with the switching state set to "0". When $\Delta T < \delta$, the switching state is "0" if ΔT is greater the triangular carrier wave, and the switching state is "−1" if ΔT is less than the triangular carrier wave.

3.3. Hysteresis Threshold Optimization

In the hysteresis control strategy, when the load torque increases, the phase current increases to maintain the torque output, leading to an increased current change rate and a higher peak current. This necessitates the maintenance of a low current peak by increasing the hysteresis threshold. When the load is small, the hysteresis threshold is reduced to improve current tracking accuracy. At high-speed operation, the increased rotor speed generates a substantial back-EMF. According to the motor voltage equation, this back-EMF opposes the applied voltage, significantly reducing the effective voltage available for driving current changes. Consequently, the current rise and fall rates are strongly inhibited, making it difficult for the actual phase current to accurately track the reference current within the required interval. The switching frequency of the hysteresis controller decreases sharply, exacerbating current distortion and leading to increased torque ripple at high speeds, so the hysteresis threshold must be increased. During low-speed operation, the extremely fast current change rate requires a reduction in the hysteresis threshold to curb switching frequency rise, thereby reducing switching losses and electromagnetic noise. Therefore, dynamic adjustment of the hysteresis threshold is crucial for optimizing system performance. The variation of the hysteresis threshold with load and speed is shown in Figure 8.

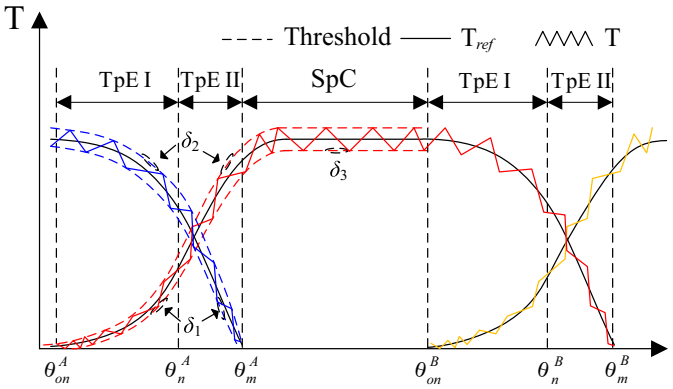

FIGURE 9. Threshold changes in different regions.

The torque variation trend within one cycle is shown in Figure 9, and the solid line, wavy line, and dashed line correspond to the reference torque T_{ref}, actual torque T, and hysteresis threshold δ, respectively. The magnitude of the hysteresis threshold is determined based on the deviation between the reference torque and actual torque.

As shown in Figure 9, during the commutation stage, the torque error varies with the rotor position, necessitating a corresponding change in the threshold value. However, under constant speed and load conditions, allowing the hysteresis threshold to vary continuously with the angle would complicate the control strategy excessively. Therefore, the hysteresis threshold for the TpE I region in the outgoing phase and the TpE II region in the incoming phase can be set to δ_1. This smaller threshold is tailored to the steep torque error gradient during initial commutation, enabling precise current tracking and minimizing transient torque ripple. For the TpE I region in the incoming phase and the TpE II region in the outgoing phase, it can be set to δ_2, and this larger threshold ($\delta_2 > \delta_1$) reduces unnecessary switching operations while still constraining the torque error within acceptable bounds during the intermediate commutation phase; in the SpC region, where the torque error is relatively small, the threshold remains constant at δ_3. This ensures stable, steady-state torque tracking and consistent switching frequency under constant speed and load conditions.

Compared with the traditional DITC strategy, which is not well-suited for varying speeds and loads, this study employs the DBO algorithm to optimize the BP neural network for predicting hysteresis thresholds under different operating conditions. The output of each layer of neurons can be expressed as Equation (6).

$$\begin{cases} u_i = x_i & \text{input layer} \\ u_j = f\left(\sum_{i=1}^{m} \omega_{ij} x_i + \theta_j\right) & \text{hidden layer} \\ u_k = f\left(\sum_{j=1}^{p} \omega_{jk} f\left(\sum_{i=1}^{m} \omega_{ij} x_i + \theta_j\right) + \theta_k\right) & \text{output layer} \end{cases} \tag{6}$$

where ω, x_i, θ_j, θ_k, and $f(x)$ are the weight, input, hidden layer threshold, output layer threshold, and activation function, respectively.

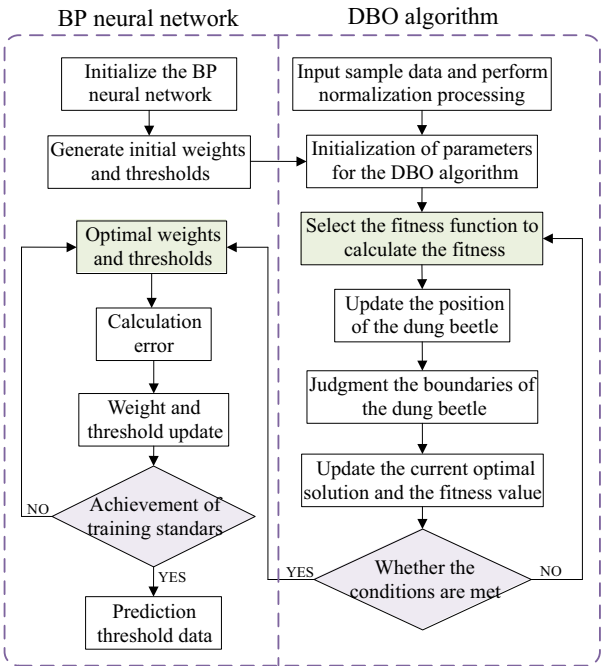

FIGURE 10. DBO-BP flowchart.

By optimizing the weight and threshold parameters of the BP neural network, the DBO algorithm effectively addresses the inherent issue of local minima in the traditional BP training process, thereby enhancing the prediction accuracy of the model. This algorithm primarily determines the globally optimal weights and thresholds by simulating and analyzing the position changes of the dung beetle.

In the DBO-BP prediction model, the input layer receives rotational speed and load as its inputs, while the output layer produces thresholds δ_1 and δ_2 as its outputs. Through the DBO-BP algorithm iterative optimization, the optimal combination of δ_1 and δ_2 is obtained for subsequent hysteresis control or modulation stages. The sampling range for rotational speed is [300 r/min, 1200 r/min] with an interval of 100 r/min, and the sampling range for load is [1 N · m, 10 N · m] with an interval of 1 N · m. A total of 100 samples were collected and subsequently divided into 75 training samples and 25 testing samples. The expression of the fitness function is given by Equation (7). The fitness function takes torque ripple minimization as the optimization objective, directly using torque ripple as the core evaluation metric. The optimization process of the algorithm is essentially the continuous reduction of torque ripple.

$$f_{fitness} = \arg\min(\alpha \cdot mes(TrainDateError) + (1-\alpha)mes(TestDateError)) \quad (7)$$

where $f_{fitness}$ is the fitness function, and *TrainDateError* and *TestDateError* represent the errors of the training set and test set. The parameter α is dynamically adjusted based on the number of iterations, with an initial emphasis on minimizing the training error while gradually increasing the weight of the test error as the iterative process advances.

The weights and thresholds of the BP neural network were optimized by employing the DBO algorithm. The optimal hysteresis threshold data under different speeds and loads were obtained through offline optimization as training samples, and the optimal hysteresis thresholds δ_1 and δ_2 were calculated using the DBO-BP algorithm based on the fitness function under the minimized torque ripple. The flowchart of the DBO-BP algorithm is shown in Figure 10.

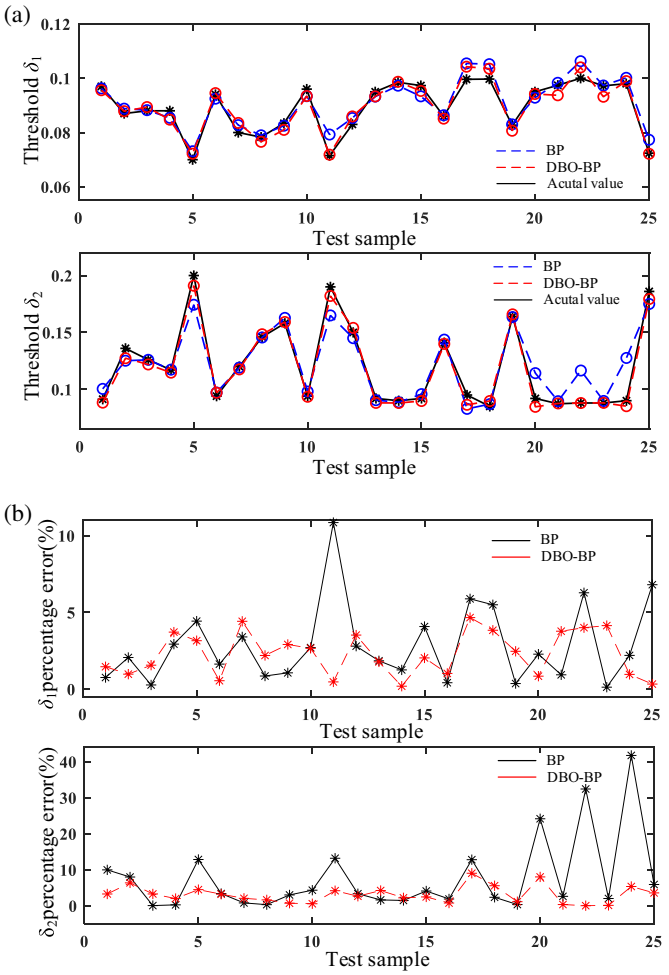

FIGURE 11. δ_1, δ_2 threshold prediction and error. (a) Threshold δ_1, δ_2 prediction; (b) Threshold δ_1, δ_2 error.

As can be seen from Figure 11(a), the prediction results of the DBO-BP model closely matched the actual values, and it showed excellent performance. A comparison is conducted between the DBO-BP and BP neural network models to validate the effectiveness of the algorithm. The DBO-BP model exhibited a smaller prediction error than the BP model, as shown in Figure 11(b).

4. SIMULATION AND EXPERIMENTATION

4.1. Simulation Analysis

The 6/20 PMa-SRM was taken as the research subject in this study, and its parameters are presented in Table 1. A simulation model used the MATLAB/Simulink software to validate the effectiveness of the subdivided variable hysteresis threshold strategy.

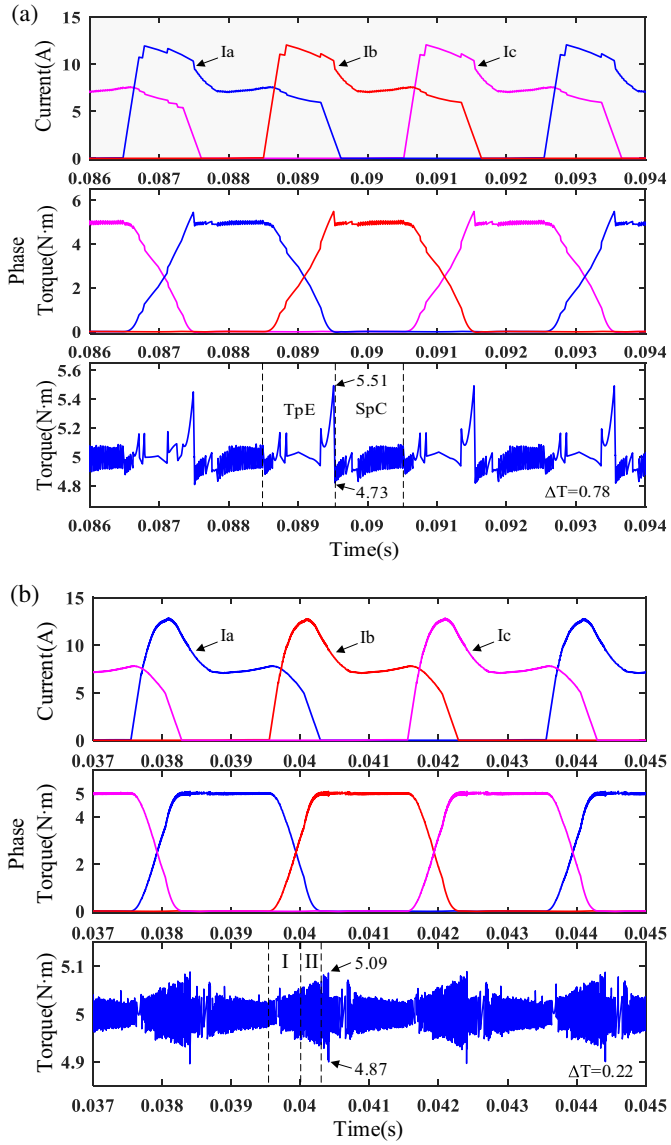

FIGURE 12. Current and torque waveforms with speed 500 r/min and load of 5 N · m. (a) Traditional DITC strategy; (b) subdivided variable hysteresis threshold control strategy.

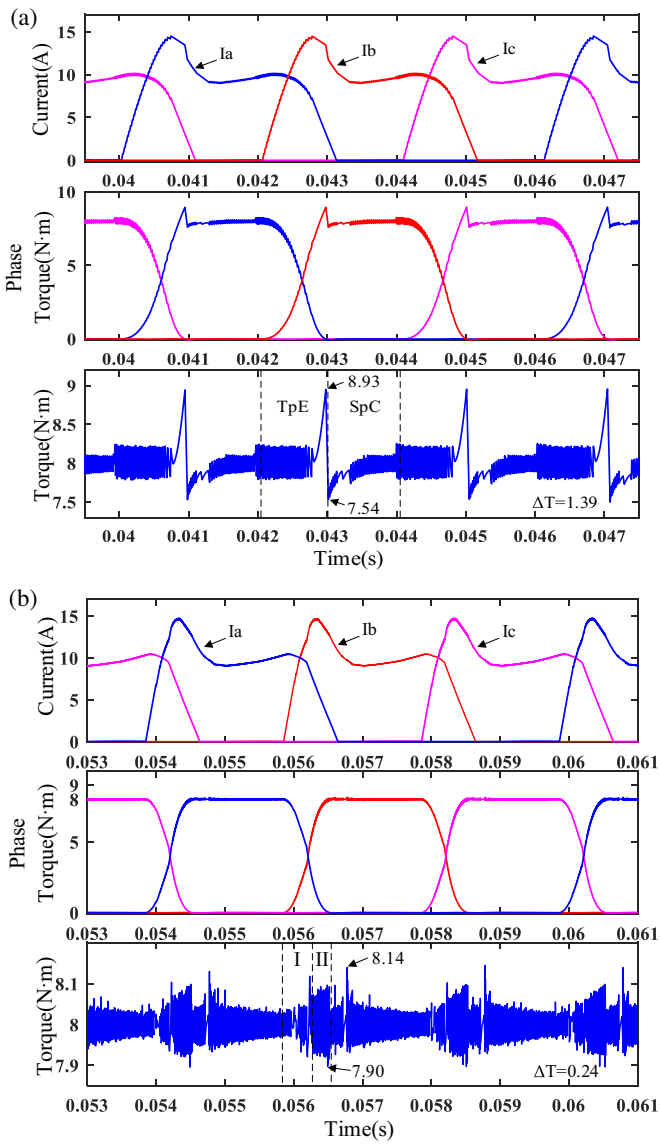

FIGURE 13. Current and torque waveforms with speed 500 r/min and load of 8 N · m. (a) Traditional DITC strategy; (b) subdivided variable hysteresis threshold control strategy.

TABLE 1. Motor parameters.

Parameters	value	Parameters	value
Stator poles	6	DC voltage/V	540
Rotor poles	20	Max current/A	30
Windings turns	55	Rated speed/rpm	1500
Stator diameter/mm	100	Resistance/Ω	0.6

The torque ripple expression is defined in (8) to analyze the torque ripple of the motor under the two control strategies.

$$T_r = \frac{T_{\max} - T_{\min}}{T_{avg}} \tag{8}$$

where $T_{\max}$ and $T_{\min}$ represent the maximum and minimum values of the three phases synthesized torque, and T_{avg} denotes the average value of the torque.

The simulation waveforms for the two control strategies at a speed of 500 r/min and a load torque of 5 N · m are presented in Figure 12. The torque range of the traditional DITC is 4.73–5.51 N · m, with a torque ripple of 15.6%. The torque range for the proposed strategy is 4.87–5.09 N · m, accompanied by a torque ripple of only 4%. The conventional DITC fixed hysteresis control strategy exhibits significant torque ripple at the boundary between the TpE and SpC regions due to the transformation of the hysteresis method. The proposed strategy introduces an additional TpE II region and employs PWM control in different regions, which reduces the torque ripple.

When the load is increased to 8 N · m, the torque ripple of the proposed strategy is 3%, and the traditional DITC strategy is 17.4%, as shown in Figures 13(a) and (b). In the traditional DITC strategy, to ensure sufficient torque during the initial state, the incoming phase of the TpE region remains the excitation state, leading to excessive current peak, and the hys-

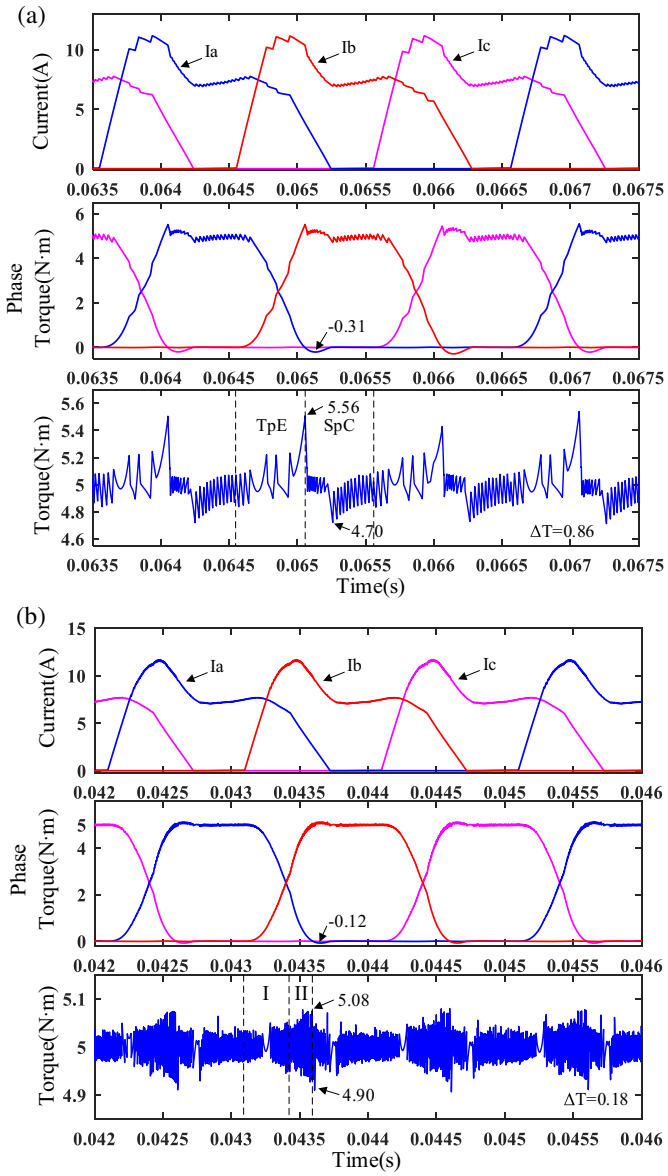

FIGURE 14. Current and torque waveforms with speed 1000 r/min and load of 5 N · m. (a) Traditional DITC strategy; (b) subdivided variable hysteresis threshold control strategy.

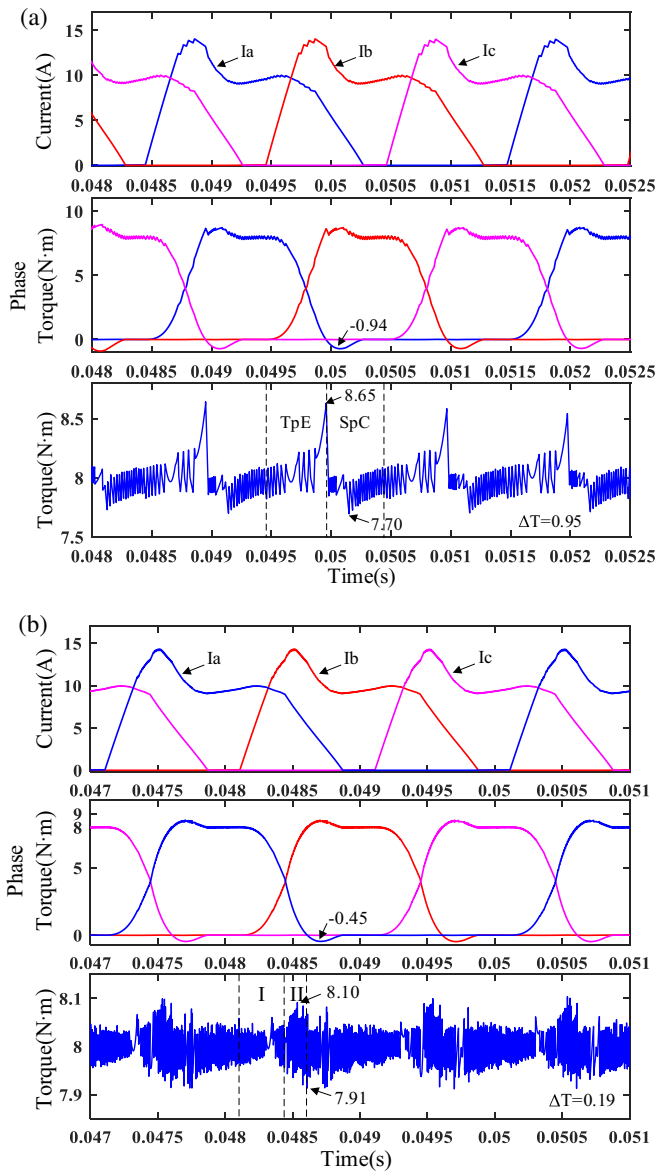

FIGURE 15. Current and torque waveforms with speed 1000 r/min and load of 8 N · m. (a) Traditional DITC strategy; (b) subdivided variable hysteresis threshold control strategy.

teresis threshold is fixed, which results in significant torque ripple. The proposed strategy achieves stable current variations across different intervals and smooth commutation transitions through precise interval division and an optimized hysteresis threshold, thereby effectively suppressing torque ripple.

To further validate the effectiveness of the subdivided variable hysteresis threshold strategy in suppressing torque ripple, simulation analyses were performed under operating conditions with a rotational speed of 1000 r/min and load torques of 5 N · m and 8 N · m. The torque and current waveforms for the traditional DITC strategy and subdivided variable hysteresis threshold strategy are presented in Figures 14 and 15, respectively. A comparison of the motor simulation results for the two control strategies is presented in Table 2.

TABLE 2. Comparison of simulation results with speed 1000 r/min, load of 5 N · m and 8 N · m.

Speed-Load	Control strategy	Total torque/N · m	Torque ripple/%
1000 r/min 5 N · m	Traditional DITC	4.70–5.56	17.2
	Proposed control strategy	4.90–5.08	3.6
1000 r/min 8 N · m	Traditional DITC	7.70–8.65	11.9
	Proposed control strategy	7.91-8.10	2.4

As shown in Figure 15, when the motor operates at a speed of 1000 r/min and under a load torque of 8 N · m, the traditional DITC hysteresis control strategy generates a significant nega-

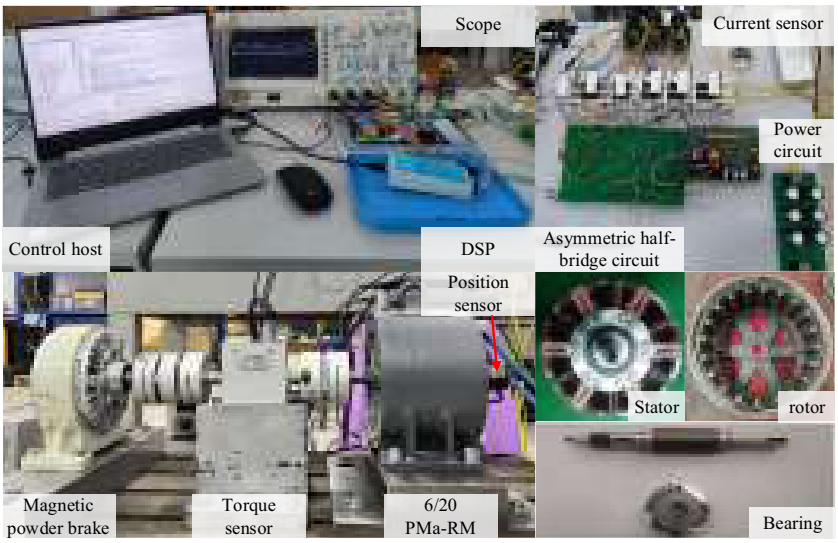

FIGURE 16. Experimental platform of 6/20 PMa-SRM.

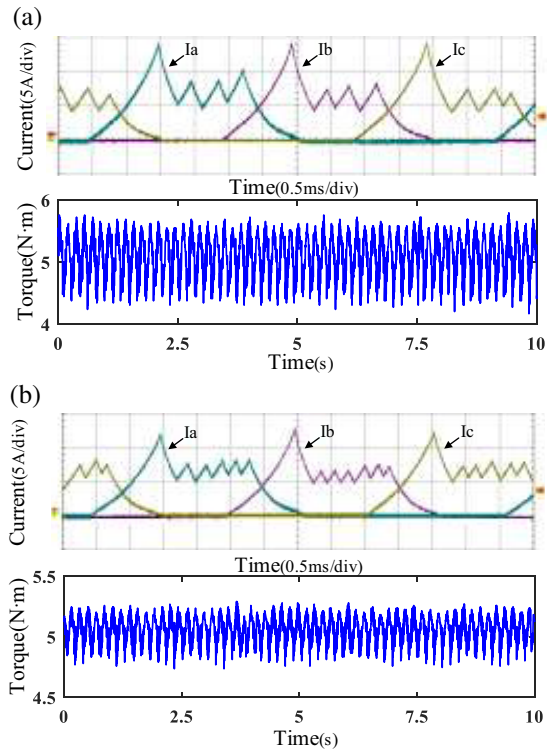

FIGURE 17. Current and torque waveforms with speed 500 r/min and load of 5 N · m. (a) Traditional DITC strategy; (b) subdivided variable hysteresis threshold control strategy.

tive torque because of the inability of the previous phase current to promptly decay to zero, thereby disrupting the balance of the total torque. The subdivided hysteresis threshold strategy enables the motor to select an optimal hysteresis threshold during the outgoing phase in the TpE region, facilitating a faster current decay to zero and effectively mitigating the negative torque. The optimal thresholds corresponding to different speeds and load conditions are listed in Table 3.

TABLE 3. The optimal thresholds under different working conditions.

Speed-Load	Threshold δ_1	Threshold δ_2
500 r/min, 5 N · m	0.07	0.083
500 r/min, 8 N · m	0.076	0.095
1000 r/min, 5 N · m	0.08	0.09
1000 r/min, 8 N · m	0.095	0.15

4.2. Experimental Analysis

As shown in Figure 16, the PMa-SRM experimental platform was established. An asymmetric half-bridge power converter is employed to drive the motor. The digital signal processing (DSP) controller utilized the TMS320F28335 chip. The chip's maximum operating frequency is 150 MHz; the PWM carrier frequency is 10 kHz; and the sampling frequency is 80 ns. The P parameter in the PI controller is 5, and the I parameter is 0.1. The DYN-200PRO torque sensor was adopted for measuring the total torque. The BRT38COM32768 absolute position encoder from BRITER Company provided real-time positional feedback of the motor, and the accuracy of this encoder can reach 0.01°. The current detection circuit monitored the motor's real-time current and fed it back to the control circuit for regulation.

As shown in Figure 17, under the operating conditions of 500 r/min rotational speed and a load torque of 5 N · m, the traditional DITC strategy exhibits a peak current of approximately 14.5 A, with a torque fluctuation ranging from 4.24 to 5.76 N · m and a torque ripple of 30.4%. In contrast, the subdivided variable hysteresis threshold control strategy reduces the peak current to 12 A, narrows the torque fluctuation to 4.74–5.29 N · m, and decreases the torque ripple to 11%.

As evidenced by the experimental results presented in Figures 17 and 18, the excitation current and demagnetization current of the traditional DITC strategy exhibit significant fluctua-

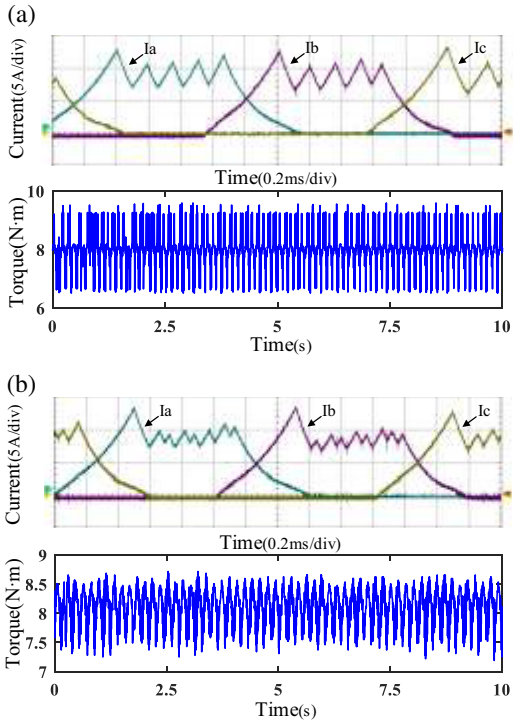

FIGURE 18. Current and torque waveforms with speed 1000 r/min and load of 8 N · m. (a) Traditional DITC strategy; (b) subdivided variable hysteresis threshold control strategy.

tions in the TpE region, leading to a substantial torque ripple. In contrast, the subdivided variable hysteresis threshold strategy introduced in this study effectively mitigates these fluctuations. As shown in Figure 17, the current fluctuation range decreases from 5 A to 3 A, indicating a more stable current variation and a marked reduction in torque ripple.

The discrepancies between experimental and simulated results are primarily attributed to non-ideal factors in the practical system. In actual experiments, the system is affected by various non-ideal conditions, such as current sampling noise, magnetic circuit saturation, and mechanical friction. These factors tend to increase the actual torque ripple, leading to a certain gap between simulated and experimental outcomes.

5. CONCLUSION

To address the issue of significant torque ripple in the TpE region of the PMa-SRM motors, this study proposes a subdivided variable hysteresis threshold torque suppression strategy. The main features of this paper are as follows.

(1) This control strategy partitions the torque current into distinct regions and employs different PWM algorithms to generate switching signals for each working region. Consequently, the total torque during commutation becomes more stable, and the transition between the TpE and SpC regions is smoothed.

(2) The hysteresis threshold is optimized using the DBO-BP algorithm, enabling the motor to adapt to various operating conditions while reducing torque ripple during operation.

(3) Simulation experiments confirm that compared with the traditional DITC strategy, the proposed control strategy effectively mitigates torque ripple during the transition between the TpE and SpC regions, demonstrating good application potential.

ACKNOWLEDGEMENT

This study was supported by the Jiangxi Provincial Key Laboratory of Maglev Rail Transit Equipment under Grant 2020SSY050 and in part by the Jiangxi Natural Science Foundation Project under 20232BAB204063.

REFERENCES

[1] Sun, X., L. Feng, K. Diao, and Z. Yang, "An improved direct instantaneous torque control based on adaptive terminal sliding mode for a segmented-rotor SRM," *IEEE Transactions on Industrial Electronics*, Vol. 68, No. 11, 10 569–10 579, 2021.

[2] Jia, W., Y. Hua, Y. Cui, X. Liu, Z. Zhang, and H. Qiu, "Comparative study of different hybrid excitation electrical machines with doubly salient poles," *Journal of Power Electronics*, Vol. 25, No. 10, 1845–1854, 2025.

[3] Fu, G. J., Y. H. Chen, and H. W. Mu, "Design and protection of the controller for SRD system," *Science Technology and Engineering*, Vol. 7, No. 22, 5886–5889, 2007.

[4] Song, S., G. Fang, Z. Zhang, R. Ma, and W. Liu, "Unsaturated-inductance-based instantaneous torque online estimation of switched reluctance machine with locally linearized energy conversion loop," *IEEE Transactions on Industrial Electronics*, Vol. 65, No. 8, 6109–6119, 2018.

[5] Cai, Y. C. and L. B. Wang, "Self-adaptive rbf neural network control theory of switched reluctance motor," *Science Technology and Engineering*, Vol. 12, No. 4, 908–910, 2012.

[6] Tian, D. X., B. N. Qu, J. C. Song, and Y. Zhao, "An analytical method of PWM duty cycle for switched reluctance motors based on current chopping control," *Transactions of China Electrotechnical Society*, Vol. 34, No. 21, 4449–4457, 2019.

[7] Deepak, M., G. Janaki, and C. Bharatiraja, "Model predictive current control improved performance on SRM drive for electric vehicles," in *2023 IEEE International Transportation Electrification Conference (ITEC-India)*, 1–6, Chennai, India, 2023.

[8] Yang, W. H., B. Gou, Y. Lei, X. X. Song, and J. Wang, "SRM torque ripple suppression method based on model predictive control," *Advanced Technology of Electrical Engineering and Energy*, Vol. 39, No. 8, 18–28, 2020.

[9] Ren, P., J. Zhu, Y. Zhao, and Z. Jing, "A novel direct torque control method for switched reluctance motors based on optimal turn-on angle," *Journal of Power Electronics*, Vol. 24, No. 9, 1417–1427, 2024.

[10] Al-Amyal, F., L. Számel, and M. Hamouda, "An enhanced direct instantaneous torque control of switched reluctance motor drives using ant colony optimization," *Ain Shams Engineering Journal*, Vol. 14, No. 5, 101967, 2023.

[11] Ben, T., H. Wang, L. Chen, Y. Zhang, and L. Jing, "Torque ripple reduction strategy for switched reluctance motor based on segmented non-linear correction torque sharing function," *Journal of Power Electronics*, Vol. 24, No. 12, 1933–1943, 2024.

[12] Han, G., Z. Lu, M. Wu, and D. Yu, "Direct instantaneous torque control method for switched reluctance motor based on an improved sliding mode control strategy," *Transactions of China Electrotechnical Society*, Vol. 37, No. 22, 5740–5755, 2022.

[13] Qing, L., H. M. Wang, and X. L. Ge, "A high efficiency torque ripple suppression method for switched reluctance motor," *Transactions of China Electrotechnical Society*, Vol. 35, No. 9, 1912–1920, 2020.

[14] Song, S., G. Fang, R. Hei, J. Jiang, R. Ma, and W. Liu, "Torque ripple and efficiency online optimization of switched reluctance machine based on torque per ampere characteristics," *IEEE Transactions on Power Electronics*, Vol. 35, No. 9, 9608–9616, 2020.

[15] Cai, Y., C. Ju, H. Wang, Y. Wan, and H. Zhang, "A new direct instantaneous torque control method of switched reluctance motor and its high efficiency operation," *Transactions of China Electrontechnical Society*, Vol. 37, No. 18, 4625–4637, 2022.

[16] Gobbi, R. and K. Ramar, "Optimisation techniques for a hysteresis current controller to minimise torque ripple in switched reluctance motors," *IET Electric Power Applications*, Vol. 3, No. 5, 453–460, 2009.

[17] Lee, Y. K., "Torque ripple and switching power loss minimization with constant band hysteresis current controller for BLDC motor," in *2019 IEEE PES Asia-Pacific Power and Energy Engineering Conference (APPEEC)*, 1–4, Macao, China, 2019.

[18] Li, L. H., L. Li, X. Wang, *et al.*, "A loss prediction model for PMSM based on BP neural network optimized by dung beetle optimizer," *Modern Manufacturing Engineering*, No. 2, 130–137, 2025.

[19] Huang, W. J., X. Y. Dong, and J. Z. Zhu, "Model predictive torque control of permanent magnet synchronous motors based on dung beetle optimization algorithm," *Small & Special Electrical Machines*, Vol. 52, No. 7, 67–71, 2024.

[20] Huang, C. Z., J. X. Xu, X. P. Liu, W. S. Cao, and Y. L. Wu, "A four region DITC method for permanent magnet assisted switched reluctance motor," *Proceedings of the CSEE*, Vol. 43, No. 6, 2438–2449, 2023.

[21] Zhu, Y., G. Zhang, and Y. Huang, "PWM-based direct instantaneous torque control of switched reluctance machine," *Transactions of China Electrotechnical Society*, Vol. 32, No. 7, 31–39, 2017.

[22] Gong, C., J. Xu, C. Huang, R. Xiao, and Y. Sun, "A torque ripple suppression strategy for the three regions PWM-DITC permanent magnet assisted reluctance motor," *Journal of Electrical Engineering*, Vol. 20, No. 1, 78–87, 2025.

[23] Zhang, W. and X. Zhang, "A method for direct instantaneous torque control of switched reluctance motor using variable hysteresis pulse width modulation," *Mechanical Science and Technology for Aerospace Engineering*, Vol. 43, No. 5, 858–864, 2024.

[24] Huang, C., Y. Wu, H. Yuan, W. Cao, and Y. Geng, "An analytic method of segmented PWM duty cycle for switched reluctance motor," *CES Transactions on Electrical Machines and Systems*, Vol. 7, No. 2, 163–170, 2023.

[25] Cheng, Y., X.-X. Cao, and Y.-L. Zhang, "Hysteresis-PWM direct instantaneous torque control of switched reluctance motor," *Electric Machines and Control*, Vol. 24, No. 8, 74–82, 2020.